JOURNAL OF MATERIALS SCIENCE 31 (1996) 6541–6553

Reverse cyclic fatigue of a hot isostatically pressed silicon nitride at 1370 °C

A. A. WERESZCZAK, T. P. KIRKLAND, M. K. FERBER
High Temperature Materials Laboratory, Oak Ridge National Laboratory, Oak Ridge, TN 37831-6069 USA

The uniaxial, reverse cyclic fatigue performance of a commercially available hot isostatically pressed silicon nitride was examined at 1370 °C in air and with a 1 Hz sinusoidal waveform using button-head tensile specimens. Specimens did not fail in less than 10^6 cycles when the applied stress amplitude was less than 280 MPa. Slow crack growth occurred at stress amplitudes $\geqslant$ 280 MPa and failure always occurred during the tensile stroke of the waveform. Multi-grain junction cavities resulted (i.e., the accumulation of net tensile creep strain) as a consequence of the reverse cyclic loading even though the specimens endured half their life under tensile stresses and the other half under compressive stresses. The presence of multi-grain junction cavities was a consequence of the stress exponent of tensile creep strain being greater than the stress exponent of compressive creep strain. Lastly, it was observed that the static creep resistance of this material improved when it was first subjected to reverse cyclic loading at 1370 °C for at least 10^6 cycles at 1 Hz. Silicon nitride grain coarsening (which was a consequence of the completion of the α to β silicon nitride solution/reprecipitation process that occurred during the history of the reverse cyclic loading) lessened the capacity for grain boundary sliding resulting in an improved static creep resistance.

1. Introduction

Strong interest continues to exist in the implementation and retrofitting of hot isostatically pressed (HIPed) silicon nitride (Si_3N_4) components into advanced gas turbine (AGT) engines [1, 2]. It is recognized that the operating efficiency of AGT engines can be increased (while fuel demands are decreased) if their permissible operating temperature is maximized. Engine power would double and fuel efficiency would increase by as much as 20% if operating temperatures can be increased to 1370 °C (2500 °F) from the 900–1100 °C range, where existing, all-metallic, AGT engines operate [3, 4]. Operating temperatures of 1370 °C are obtainable through the implementation of mature, structural ceramic components made from materials such as HIPed Si_3N_4, provided that the service stresses are appropriately low.

In service, the components in AGT engines are subjected to both thermal and mechanical loading in a cyclic fashion. The stress states that result from this can become quite complex in nature. In an effort to predict the performance of HIPed Si_3N_4 AGT engine components, designers and engineers have made preliminary inroads into the successful lifetime prediction of HIPed Si_3N_4 components using available high temperature static creep and tension–tension cyclic fatigue data on these materials. However, the mechanical stress state of an AGT component in service is most realistically represented by reverse cyclic or tension–compression loading. Unfortunately, high temperature, reverse cyclic fatigue engineering data on HIPed silicon nitrides are currently not available for designers and engineers to use.

Little is known about the high temperature, reverse cyclic fatigue performance of other silicon nitrides and nothing is known about how HIPed Si_3N_4 performs under such a loading condition. Several studies over the years have focused on the high temperature, tensile static creep performance [5–8] of various commercial grades of HIPed silicon nitrides while fewer studies have involved the examination of their high temperature tension–tension fatigue performance [9, 10]. Studies involving reverse cyclic fatigue at elevated temperatures of silicon nitride are also rare in the literature [11, 12] and none were found involving the testing of any HIPed silicon nitrides. In one reverse cyclic fatigue study at elevated temperatures, Masuda *et al.* [11] conducted tests at 1000 °C on a gas pressure sintered (GPS) silicon nitride and reported that the fatigue limit or ultimate stress amplitude decreased as the test temperature increased from room temperature up to 1000 °C at a test frequency of 20 Hz. However, when the ultimate stress amplitude to tensile strength ratio for the GPS silicon nitride in that study was examined it was found to have increased from $\sim$ 0.6 at room temperature to $\sim$ 0.95 at 1000 °C. Annealing effects on the reverse cyclic fatigue performance were also investigated [12] on a GPS silicon nitride at

0022–2461

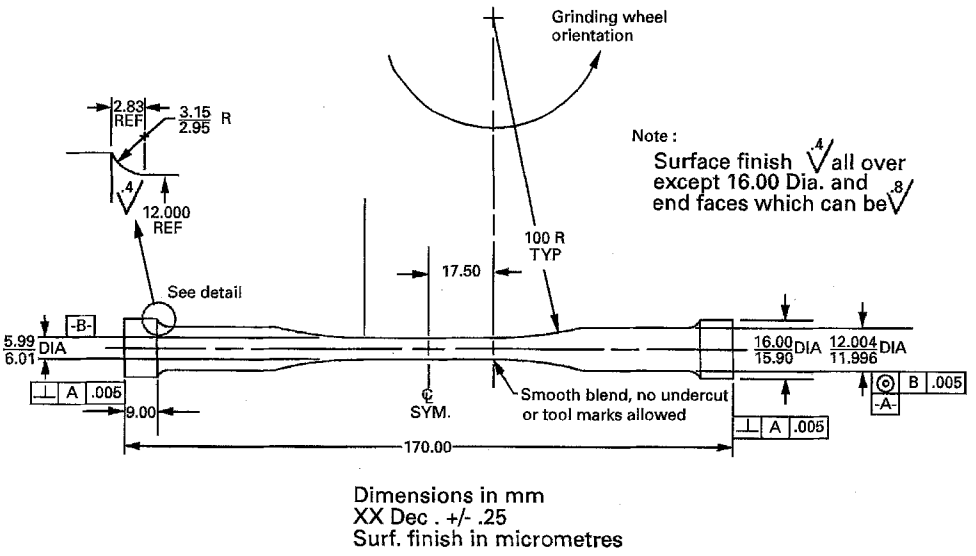

Figure 1 Dimensions of the NCX-5102 silicon nitride button-head tensile specimen used.

1000 °C and it was found that preannealing (a process that reportedly healed surface-machining damage) the material increased the material's ultimate stress amplitude. It is noted though that GPS silicon nitrides can mechanically perform quite differently than HIPed silicon nitrides, [13] so caution must be exercised when extending engineering data or performance trends to other silicon nitrides that are fabricated by other routes.

The motive of the present study was to gain an insight into how a commercially available HIPed silicon nitride mechanically performs at an elevated temperature (isothermal – 1370 °C) in air under reverse cyclic loading conditions (1 Hz, $R = \sigma_{max}/\sigma_{min} = -1$, sinusoidal waveform) in addition to examining how the number of cycles to failure depended on the stress amplitude. The change in state of the material that was a consequence of the reverse cyclic loading was also studied.

2. Material and test procedures

2.1. NCX-5102 silicon nitride

The material examined in this study was a commercially available, yttria-fluxed, hot isostatically pressed (HIPed) silicon nitride, designated by the manufacturer (Saint-Gobain/Norton Industrial Ceramic Company) as NCX-5102. The method by which this material was fabricated included an innovative closed-loop process of uninterrupted colloidal processing, from milling to shape forming, which effectively circumvented the introduction of traditional sources of contamination [14] however, 4 wt % yttria was added as a sintering aid. The powder blend was pressure slip cast to near net-shape, then glass encapsulated, and then HIPed at 210 MPa (30 ksi) between 1700–1950 °C. Grain boundary devitrification of the silicon-yttrium oxynitride phase was not promoted through any annealing treatment. After machining, the button-head tensile rods were subjected to a heat treatment (982 °C for 20 h) to oxidize (i.e., blunt) surface and near-surface flaws that may have been caused by the specimen machining. The dimensions of the final geometry of the button-head tensile specimens are shown in Fig. 1.

The microstructures of the as-received silicon nitride specimens consisted of acicular-shaped grains (typically ~ 0.7–1.5 μm × 4–10 μm) mixed with equiaxed grains (~ 0.5 μm diameter). X-ray diffraction (XRD) was conducted and an α/β Si_3N_4 ratio of 0.29 was determined [15] for the as-received material. No secondary crystalline phases were observed.

For NCX-5102 silicon nitride, the manufacturer reports the following [14]: average tensile strengths after heat treatments as high as 811 and 480 MPa at 25 and 1370 °C, respectively; average flexure strengths of 972 and 561 MPa at 25 and 1370 °C, respectively; and a fracture toughness that ranged between 5.7–6.5 MPa $m^{1/2}$ at 25 °C.

2.2. Mechanical tests

An Instron model 1332 servohydraulic test machine was used in closed-loop load control for the reverse (axial "push-pull") cyclic fatigue testing. The test system used had a fatigue rating of ± 122 kN. A 50 kN load cell was used for load monitoring and feedback control. Tension–compression grips were used in the load train for the reverse cyclic testing. A schematic of the positioning of the load train, grips, the specimen, and the furnace is shown in Fig. 2. The furnace that was used provided a 50 mm, resistance-heated hot zone which maintained 1370 °C ± 10 °C throughout the specimen's 35 mm – long gauge length. A high temperature extensometer was not used to measure the accumulation of strain during testing because concern existed that the applied large number of cycles would damage such an instrument.

Strain gauged tensile specimens were used with the tension–compression grips in order to minimize bending through suitable axial and concentricity adjustments. Specimens were commercially strain

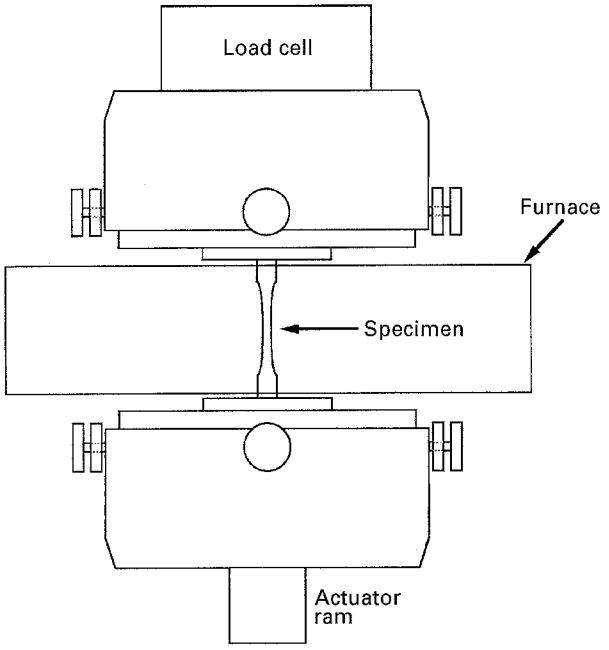

Figure 2 Schematic of the load train, specimen grips, specimen, and furnace arrangement used in the reverse cyclic fatigue tests at 1370 °C.

gauged (HiTec Corp., Westford, MA) with the orientation shown in Fig. 3. A total of eight strain gauges were required for each specimen. Four strain gauges (numbered 1–4 in Fig. 3) mounted around the centre circumference of the gauge section were used for monitoring axial bending. The remaining four strain gauges (numbered 5–8 in Fig. 3) were used for monitoring the concentricity of the gauge section. The per cent bending was continuously calculated during the alignment procedure using a commercially available front-end processor/conditioning system (Daytronics System 10 DataPAC 10K4T-D with 10A73-4 Quad 1/4 and 1/2 bridge strain conditioner card, 10CJB-5 bridge completion card, 10A60-4 quad voltage conditioner card, and PC serial interface, Daytronic Corp., Miamisburg, OH). Schematics of axial and concentric misalignment are shown in Fig. 4. It is clearly evident that four strain gauges are insufficient to independently monitor both types of bending.

The operation and use of the tension–compression grips were co-ordinated with the strain output from the eight strain gauges. A sectioned view of the tension–compression hydraulic grips (Patented by the Instron Corporation, Canton, MA) is shown in Fig. 5. Once the strain gauged specimen was mounted in the upper and lower grips, the adjustments for axial and concentric bending were made with the vertically-oriented, large set screws and horizontally-oriented thumbwheels, respectively, that are shown in Fig. 5. The upper grip was aligned with the test frame's upper cross-beam and load cell by the manufacturer and was never readjusted; all bending minimization was conducted via adjustment of the bottom grip. Hydraulic actuation in the tension–compression grips applied the compressive load to the ends of the button-head specimen, while the copper collets and face plates shown in Fig. 5 constrained the specimen during the tensile stroke of the waveform. By minimizing axial and concentric misalignment of the mounted specimen (see the schematic in Fig. 6), the two types of bending were reduced to less than $\pm$ 5% at the maximum tension and compression stresses. It has been reported that up to 5% bending can be tolerated in tension tests [16]; tensile bending becomes the limiting bending condition in tension–compression tests because ceramics are much more susceptible to bending-induced stress failure in tension than in compression.

The steps in testing the reverse cyclic fatigue specimens were:

(1) A strain gauged NCX-5102 specimen was mounted in the upper grip with the strain gauges numbered 1–4 aligned with the set screws (and thumbwheels) on the upper grip; the strain gauges were also in alignment with those on the lower grip.

(2) The outputted strain values from the strain gauges were zeroed. The specimen was mounted on the bottom grip with the actuator in position control.

(3) The test machine was placed into load control with a preload of approximately + 200 N ($\sim$ + 7 MPa).

(4) The load was incrementally increased in steps of + 1000 N ($\sim$ + 35 MPa) to the desired stress for testing, while both axial and concentric bending were minimized at each step.

(5) The load was returned approximately + 200 N and the compressive-loading piston (shown in Fig. 5) was applied to the ends of the specimen while in load control.

(6) Axial and concentric bending were checked in $\pm$ 1000 N increments to the desired maximum compressive and tension load. It was found that if axial and concentric adjustments produced very low bending in step No. 4. (e.g., less than $\pm$ 1%), then bending in compressive loading required no (or minimal) minimization.

(7) A zero load was applied to the specimen, the strain gauges were removed (including all adhesive used to mount the gauges), the specimen's gauge section was cleaned with a solvent, and the furnace was positioned into place and heated to 1370 °C.

(8) A 1 Hz sinusoidal waveform, with one of the stress amplitudes shown in Table I, was applied to the specimen after the furnace reached thermal equilibrium. The mean stress was zero and $\sigma_{max}/\sigma_{min} = -1$. If the specimen did not fail before approximately 10^6 cycles ($\sim$ 280 h), then it was interrupted and one of two actions was taken: (i) it was step stressed in $\pm$ 10 MPa increments (and cycled at each new stress amplitude for several days) until failure was produced, or (ii) it was static creep tested at 1370 °C and 125 MPa to examine the material's creep rusistance after the cyclic loading. The accumulation of creep strain that occurred in creep-rupture specimens was continuously measured using a high temperature contact extensometer.

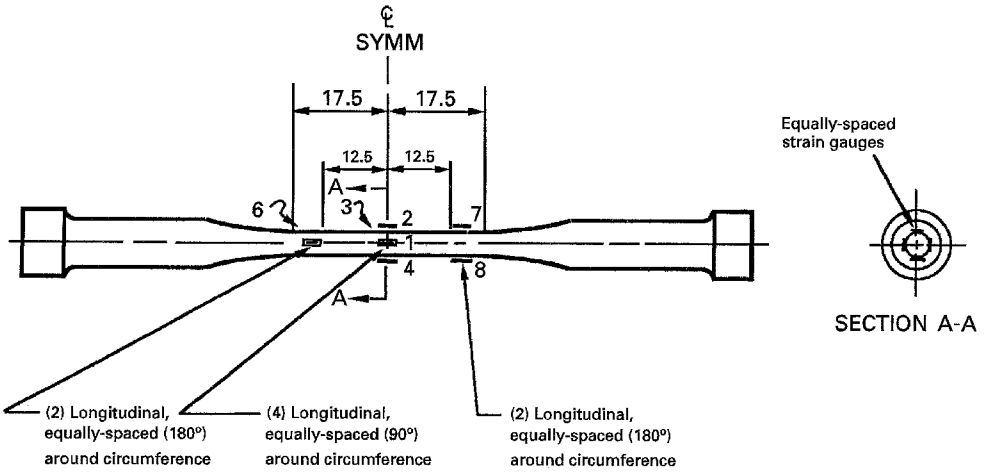

Figure 3 Positioning of the eight strain gauges used to monitor axial and concentric bending on each specimen.

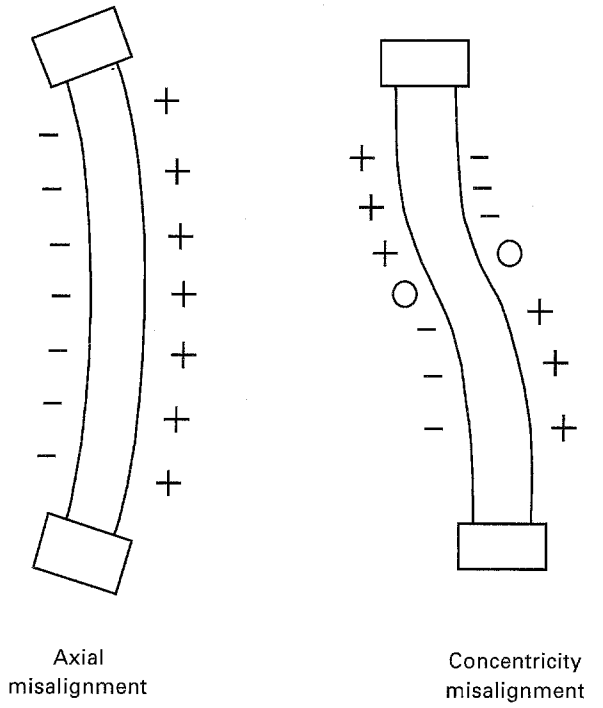

Figure 4 Two categories of bending misalignment that were corrected for.

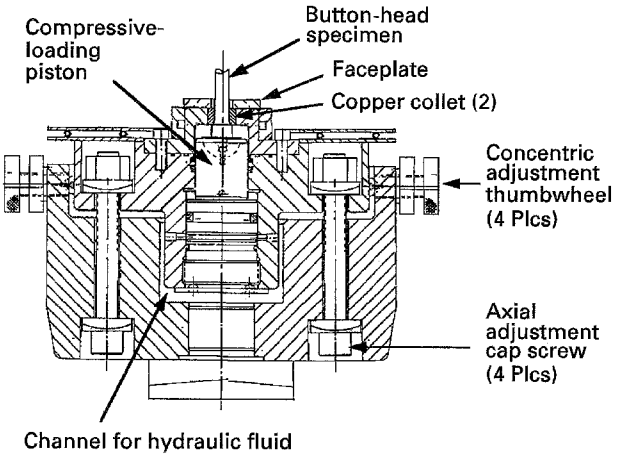

Figure 5 Sectioned view of one of the two specimen grips used for the reverse cyclic loading. The adjustment of four thumbwheels and four cap screws correct for concentric and axial bending, respectively. (Drawing used with permission of Instron Incorporated, Canton, MA, USA.)

2.3. Post-testing analysis

All generated fracture surfaces were examined using optical microscopy. Scanning electron microscopy (SEM) was also used to examine the microstructures of failed specimens. Because of the generated failures at 1370 °C, the microstructure of the original fracture surface was heavily oxidized and thus inhibited its examination. However, this problem was circumvented by regenerating another fracture surface at room temperature within the failed specimen's gauge section; the new microstructure that was observed was within ~ 3 mm of the original fracture surface. The revealed microstructure on the refractured surface was deemed representative of the microstructure on the original fracture surface. X-ray diffraction (XRD) was also performed on tested specimens to identify any changes in the crystallinity of the material.

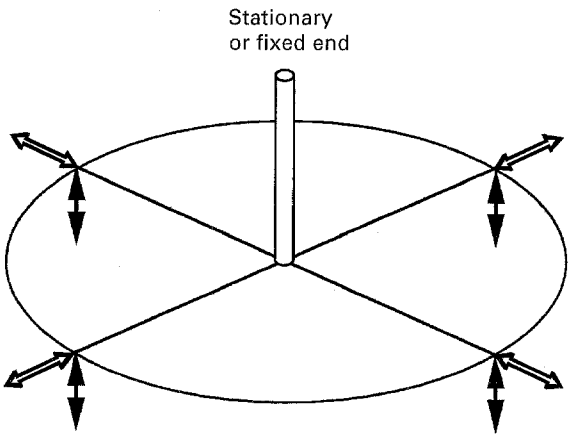

Figure 6 Adjustments in the transverse and longitudinal planes, with respect to the longitudinal axis of the button-head tensile specimen, to correct for (⇔) concentric and (↕) axial bending, with 4 places each respectively.

TABLE I Cyclic loading histories of tension–compression cyclic fatigue specimens at 1370 °C. 1-Hz sinusoidal (R = − 1) waveform used

Specimen ID	Stress (MPa)	Number of cycles at stress	Comments or Course of action
NCX-63	± 100	170 701	Interrupted – Stress increased
	± 110	273 687	Stress increased
	± 120	321 616	Stress increased
	± 130	283 164	Stress increased
	± 140	321 125	Stress increased
	± 150	260 645	Stress increased
	± 160	341 521	Stress increased
	± 170	265 263	Stress increased
	± 180	343 954	Stress increased
	± 190	255 256	Stress increased
	± 200	259 403	Stress increased
	± 210	365 328	Stress increased
	+ 220	253 334	Stress increased
	± 230	339 139	Stress increased
	± 240	173 250	Stress increased
	± 250	192 777	Stress increased
	± 260	320 995	Stress increased
	± 270	197 301	Stress increased
	± 280	260 132	Stress increased
	± 290	39 054	Failed
NCX-50	± 290	2018	Failed
NCX-51	± 250	1037 258	Interrupted and creep tested at 1370 °C/125 MPa
NCX-93	± 270	1037 258	Interrupted and creep tested at 1370 °C/125 MPa
NCX-96	± 280	81	Failed
NCX-57	± 280	1036 640	Interrupted – stress increased
	± 290	76 631	Stress increased
	± 300	80 600	Stress increased
	± 310	181 800	Stress increased
	± 320	75 688	Stress increased
	± 330	23 600	Failed
NCX-62	± 300	1009 127	Interuped – stress increased
	± 310	3425	Failed

3. Results and discussion

3.1. Cycles of failure as a function of stress amplitude

The first specimen tested (specimen NCX-63) under reverse cyclic loading at 1370 °C was subjected to a relatively low initial stress amplitude, and then step-stressed for two reasons: (1) to ensure that the test hardware was functioning properly because this was the first time that this type of test had been conducted on this machine at these elevated temperatures, and (2) to determine an approximate stress amplitude range where failure would be produced. The test was initiated at ± 100 MPa and the stess was incrementally increased by ± 10 MPa until failure was ultimately produced (after 2–4 days at each respective stress amplitude) at ± 290 MPa. The history for this test, and all other tests, is described in Table I.

A stress amplitude of ± 290 MPa (specimen NCX-50) was chosen next and failure was produced after 2018 cycles. This specimen, and all specimens that failed during reverse cyclic loading, failed during the tensile stroke of the sinusoidal waveform. The initial stress amplitude was reduced to ± 250 MPa for the third specimen tested (NCX-51) in an effort to produce a failure after a greater number of accumulated cycles; however, it did not fail after ~ 10^6 cycles. This specimen (and others) that did not fail after ~ 10^6 cycles were interrupted in the interest of test-time management.

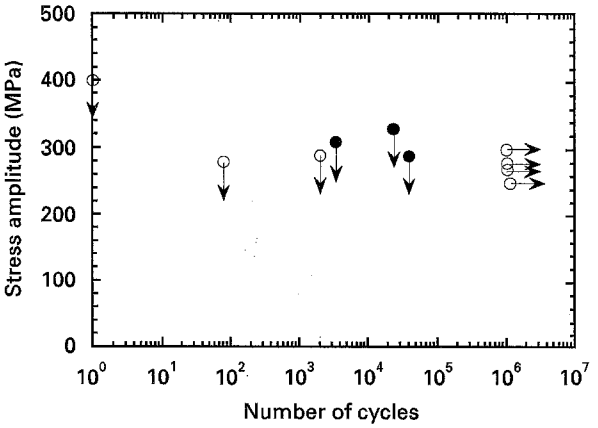

Figure 7 Cycles to failure as a function of stress amplitude for NCX-5102 silicon nitride at 1370 °C. Open circles with vertical arrows denote fatigue failures with the chosen initial stress, open circles with horizontal arrows denote runouts (no failure), and dark circles denote failure of specimens subjected to higher step-stressing after they had runout. Table I contains the loading and cycle history of each test. The open circle at 10^0 cycles represents the fast fracture tensile strength of NCX-5102 measured at 1370 °C.

The remaining four specimens were reverse cyclic fatigued starting with initial stress amplitudes ranging between ± 270– ± 300 MPa. Of the seven total specimens tested, only two specimens failed with the chosen initial stress amplitude (NCX-50 and NCX-96) and are denoted in the stress amplitude–number of cycles to failure (S–N) curve Fig. 7 by the open circles with the

vertical arrows (the open circle with the vertical arrow at 10^0 cycles represents a fast fracture strength test that was conducted on this material at 1370 °C). Four of the specimens (NCX-51, -57, -62 and -93) did not fail after 10^6 cycles and were interrupted; they are denoted by the open circles in Fig. 7 with the horizontal arrows. Of these four specimens, specimens NCX-57 and NCX-62 were subjected to further increases in stress amplitudes until cyclic fatigue failure was produced; they are denoted in Fig. 7 by the dark circles having vertical arrows (along with specimen NCX-63). As was previously discussed, the failure of NCX-63 was produced after a lengthy duration of increasing stress amplitude. Specimens NCX-51 and NCX-93 were subjected to static creep rupture testing and the results of those tests will be discussed momentarily.

The results of the reverse cyclic loading of NCX-5102 silicon nitride at 1370 °C indicate that specimens or components made from this material will not fail for durations less than 10^6 cycles, provided (1) the applied stress amplitude is less than $\pm$ 280 MPa and (2) a 1 Hz sinusoidal waveform is applied. This ultimate stress amplitude is $\sim$ 60% of the manufacture's reported average tensile strength at this temperature for this HIPed silicon nitride [14]. A similar stress amplitude was found to describe the reverse cyclic fatigue limit for a gas-pressured sintered silicon nitride at 1000 °C tested at 1 Hz. Due to limitations in the number of specimens in the test matrix in the present study, a more systematic construction of the S–N curve in Fig. 7 was not obtained.

3.2. Cavity formation during reverse cyclic fatigue

Frequently, lenticular-shaped cavities are visible in the microstructures of HIPed silicon nitride specimens that are creep ruptured at this temperature [5]. However, they were not consistently found in any of the microstructures of specimens that failed during cyclic fatigue in the present study. Typical microstructures of tested material are shown in Fig. 8(a and b) (specimen NCX-62) and show no evidence of the presence of lenticular cavities. However, even though lenticular cavities were not present, a conclusion that cavitation did not occur cannot be made because the much larger, multi-grain junction cavities are not easily discerned on refractured microstructures such as that shown in Fig. 8.

Tensile creep strain is not symmetric to compressive creep strain in most structural ceramics containing a viscous secondary phase because the stress exponent for the accumulation of tension creep strain is typically higher than that for accumulated compression creep strain, including HIPed silicon nitrides [17]. A tensile stress exponent of 3.6 has been reported by the authors for NCX-5102 at 1370 °C [18]. Although the compressive stress exponent for creep is unknown for this material, it is believed to follow Nabarro–Herring creep behaviour with a compressive stress exponent equalling one [17]. The understanding of the total creep strain becomes complicated when reverse cyclic loading is applied because of the differences in

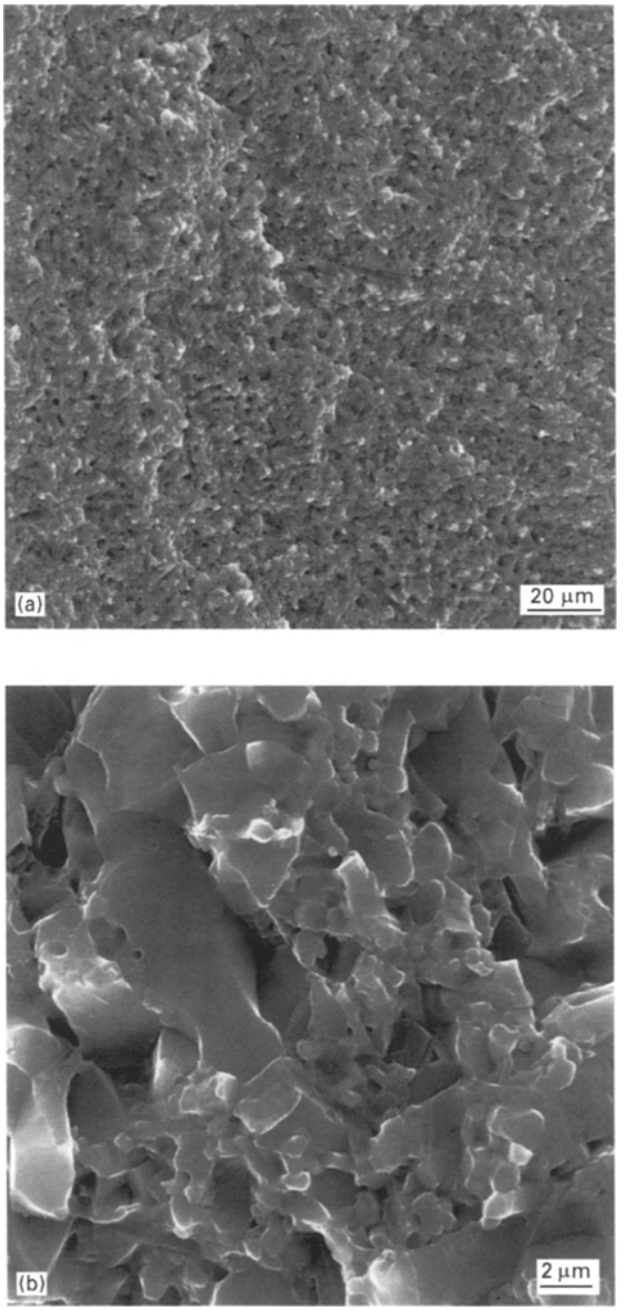

Figure 8 Microstructure of NCX-62 at (a) relatively low, and (b) high magnifications. NCX-62 failed during cyclic fatigue at 1370 °C. Refractured surface shown.

the stress exponents in tension and compression. However, being that the stress exponent of tensile creep is greater than the stress exponent of compressive creep, there should be a net gain of tensile creep strain; this is supported by what is shown in Fig. 9 (a and b). A polished cross-section of specimen NCX-57 was prepared and plasma etched. It should be noted that Plasma etching preferentially attacks the silicon nitride grains, which accentuates the yttrium-silicon-oxynitride grain boundaries. Multi-grain junction cavities and pores are visible in Fig. 9(a) and are a consequence of the net accumulation of tensile creep strain. Cavitation can account for as much as 85% of the total accumulated creep strain in HIPed silicon nitrides [19]. A polished and plasma etched surface of virgin material is shown in Fig. 9(b) for comparison: notice the lack of cavities and pores. Even though

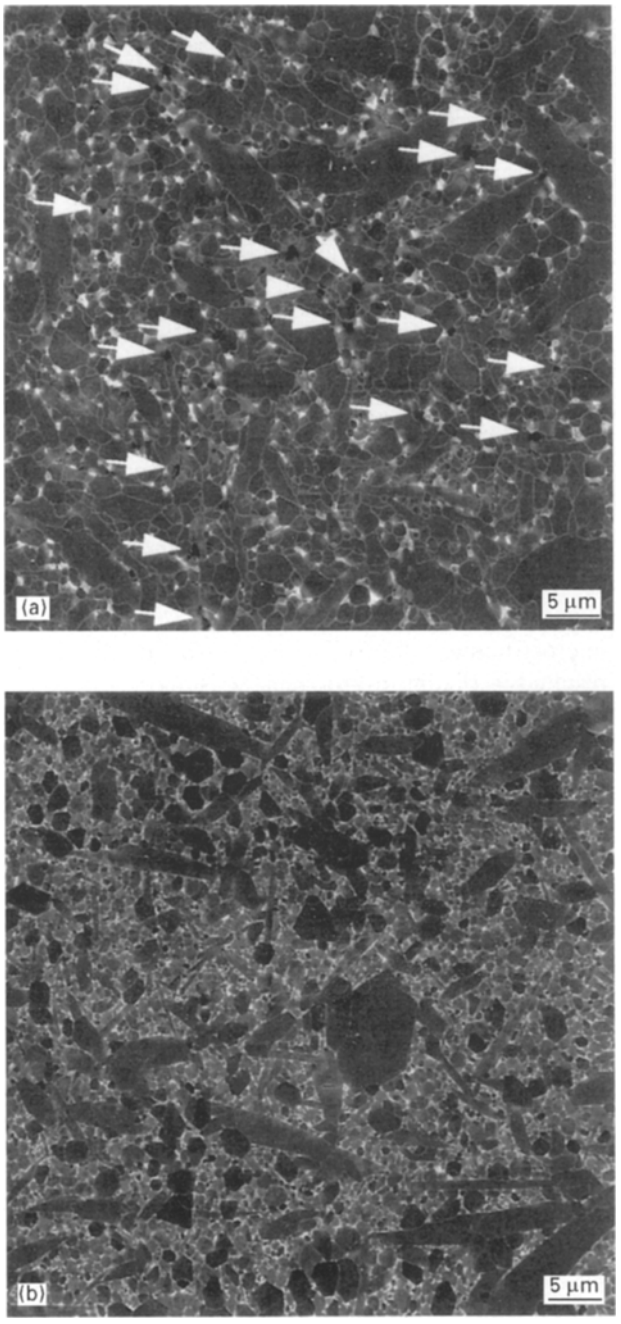

Figure 9 Polished and plasma-etched surfaces of (a) NCX-57, cyclic fatigued until failure at ± 330 MPa, and (b) virgin NCX-5102 silicon nitride material. Multi-grain junction cavities and pores are visible in (a) and this represents the accumulation of tensile creep strain, even though the specimen spent half its life under compressive stresses. Arrows in (a) show multi-grain junction cavities.

cavitation resulted as a consequence of the reverse cyclic loading at1370 °C, it did not appear to be detrimental to the creep resistance and specimen lifetime when cyclic loaded specimens (NCX-51 and NCX-93) were later creep ruptured. A discussion on this point follows.

3.3. Effect of cyclic loading on static creep performance

Specimens NCX-51 and NCX-93 (which were subjected to reverse cyclic loading) exhibited greater creep resistance than a virgin NCX-5102 specimen (NCX-40), as evidenced by the creep histories shown in Fig. 10(a). Specimens NCX-51 and NCX-93 had lon-

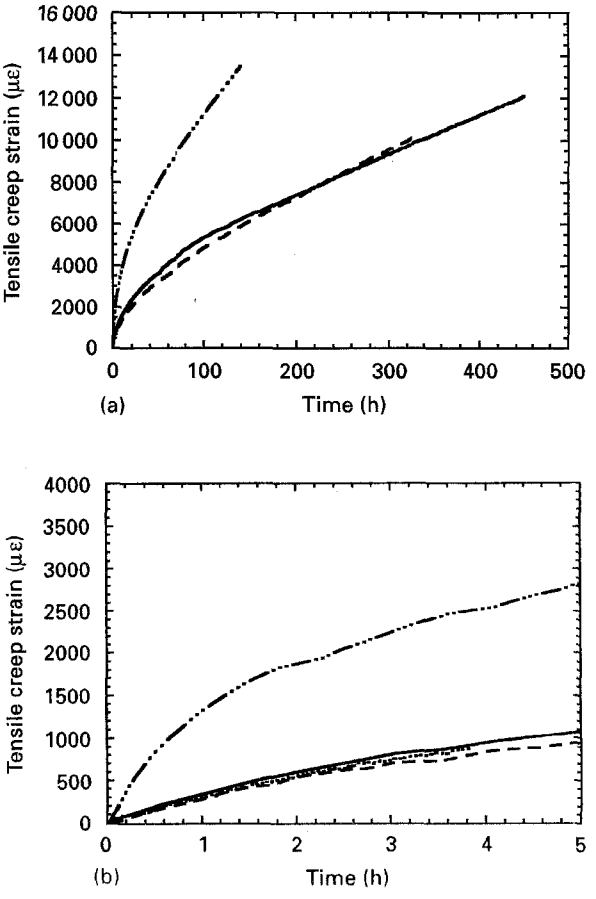

Figure 10 Whole (a) and early hour (b) creep histories of NCX-5102 specimens (— - - -) NCX-40, (— — —) NCX-51 (T–C), (——) NCX-93 (T–C) and (- - -) NCX-111 (T–T) subjected to static creep-rupture tests. "T–C" and "T–T" denote that the specimen was previously subjected to either tension–compression or tension–tension cyclic loading, respectively. Specimen NCX-40 and not subjected to any previous loading history prior to its creep–rupture testing.

ger times to failure (333 and 448 h, respectively) and slower minimum creep rates (6.2 and $4.4 \times 10^{-9}\,s^{-1}$) than specimen NCX-40 (time to failure was 140 h and the minimum creep rate was $1.6 \times 10^{-8}\,s^{-1}$). It is evident that any creep strain that accumulated during the reverse cyclic loading of specimens NCX-51 and NCX-93 was not a detriment to their lifetimes. A specimen designated as NCX-111 was subjected to tension–tension cyclic fatigue at 1370 °C using a 0.1 Hz triangular waveform, R = 0.1 and a maximum tensile stress of 125 MPa. The specimen was interrupted after 3161 h and after it had accumulated 1.67% of creep strain (i.e., strain ratchetting).

Specimen NCX-111 was subjected to static creep testing at 1370 °C and 125 MPa similarly to specimens NCX-51 and NCX-93, but it exhibited a lifetime of only 3.8 h (shown in Fig. 10(b)) This evidence strongly suggests that the previously accumulated creep strain resulted in the shorter static creep lifetime of NCX-111.

The improved static creep resistance (exhibited by specimens that were first subjected to a history of reverse cyclic loading) was a consequence of (1) grain growth and grain interlocking associated with the transformation of residual α silicon nitride and β phase through a solution/reprecipitation process, and (2) the fact that insignificant creep deformation

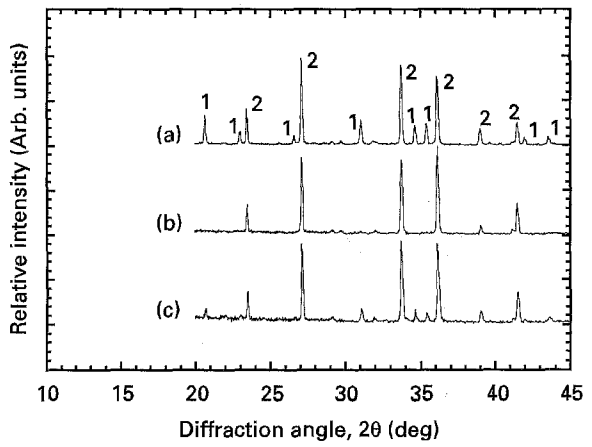

Figure 11 X-ray diffraction spectra for the (a) as-received material (from untested NCX-57), (b) material that was subjected to only a history of reverse cyclic loading (from tested NCX-57) and (c) material that was only subjected to static creep testing (from tested NCX-40). Only the history of the reverse cyclic loading was associated with the complete transformation of α and β silicon nitride. The label (1) denotes αSi_3N_4 (JCPDS 9-250), label 2 denotes βSi_3N_4 JCPDS 33-1160.

had occurred during reverse cyclic loading. Interlocking or pinning of equiaxed grains by networked, acicular grains is known to improve creep resistance [20]. In addition, an improvement in creep resistance is observed (provided that extensive cavity nucleation and growth are not active) if the grain size of equiaxed matrix grains is increased in a material system in which the equiaxed grains are mixed with larger, acicular-shaped grains [21]. The presence of residual α silicon nitride was associated with poorer creep resistance because the grain size of this initial phase was small and there was a lack of grain interlocking and grain boundary sliding could readily occur. X-ray diffraction spectra that show the changes in the α/β silicon nitride ratio are shown in Fig. 11. The as-received NCX-5102 silicon nitride had a measured α/β silicon ratio of 0.29. When specimens were subjected to only a history of reverse cyclic loading, the value of the α/β silicon nitride ratio lessened and approached zero (see the middle spectrum in Fig. 11). It cannot be concluded whether the cyclic loading at 1370 °C, or the time spent at 1370 °C, or a combination thereof, caused the thorough transformation from the α and β silicon nitride phase.

The creep resistance of a HIPed, 100% β, NCX-5102 silicon nitride is better than NCX-5102 silicon nitride containing residual α phase. Specimens NCX-51 and NCX-93 were composed of 100% β silicon nitride prior to their static creep rupture testing (because they were each exposed to a previous history of reverse cyclic loading). The poorer static creep resistance of specimen NCX-40 (compared to NCX-51 and NCX-93) was associated with its high initial α silicon nitride content prior to its testing (and its associated small gain size and lack of grain interlocking) and the incomplete transformation to the β phase prior to its failure. The coarser grain microstructure associated with the reverse cyclic loading history is shown in Fig. 12(a) and is compared to the as-received material shown in Fig. 12(b). The high residual α silicon nitride content is associated with the finer grain microstructure between the large acicular grains in Fig. 12(b), while the completion of the solution/reprecipitation leading to the presence of 100% β silicon nitride is associated with the coarser, interlocking grain microstructure in Fig. 12(a). The contrast of the micrograph images shown in Fig. 12(a and b) was inverted to better show the changed microstructure and this is shown in Fig. 12(c) and (d), respectively.

Specimen NCX-40 (which had a poorer creep resistance) had an initial grain microstructure prior to its static creep rupture testing similar to that shown in Fig. 12(b or d). Specimens NCX-51 and NCX-93 had a grain microstructure similar to Fig. 12(a or c) after being subjected to a reverse cyclic loading history, but prior to their static creep testing; this coarser grain structure (and more extensive grain interlocking) resulted in the improved creep resistance. Grain boundary sliding during creep was more difficult for the microstructure shown in Fig. 12(a or c) than the microstructure shown in Fig. 12(b or d), which resulted in the improved creep resistance.

For NCX-5102, the presence of residual α silicon nitride appears to be associated with a greater amount of accumulated creep strain in the primary creep regime and an ever-decreasing creep rate in the secondary creep regime. The amount of accumulated creep strain is significantly more for specimen NCX-40 than for specimens NCX-51, and NCX-93 (as seen in Fig. 10(b)), during the first few hours of the static creep test because grain boundary sliding can occur more readily. In addition, the secondary creep rate is continually decreasing for specimen NCX-40, while the secondary creep rates of specimens NCX-51 and NCX-93 are essentially constant. As long as α silicon nitride is present (as it was throughout the history of specimen NCX-40), and as more α silicon nitride continually goes into solution and reprecipitates out as the β phase during the static creep rupture test, the creep rate will continue to decrease as a consequence. The secondary creep rate for specimen NCX-40 shown in Fig. 10(a) would have probably continued to decrease and ultimately reach a relatively constant value had it not failed before all the α phase had transformed to the β phase. Specimens NCX-51 and NCX-93 were 100% β silicon nitride prior to the commencement of their static creep testing, thus (1) the grain coarsening and interlocking process had already been saturated, (2) the accumulation of extensive creep strain during primary creep was never attained, and (3) the subsequent secondary or steady-state creep rates remained relatively constant up to the time of specimen fracture.

Although the presence of residual α silicon nitride was associated with poorer creep resistance and shorter lifetimes at 1370 °C and 125 MPa, its presence in an initial component made from this material conceivably may be advantageous under a special circumstance. If a component made from virgin NCX-5102 silicon nitride (with its high residual α silicon nitride content) is subjected to a high stress concentrator in service (e.g., an intrinsic or extrinsic flaw, a high contact stress, etc.) then the poorer creep deformation

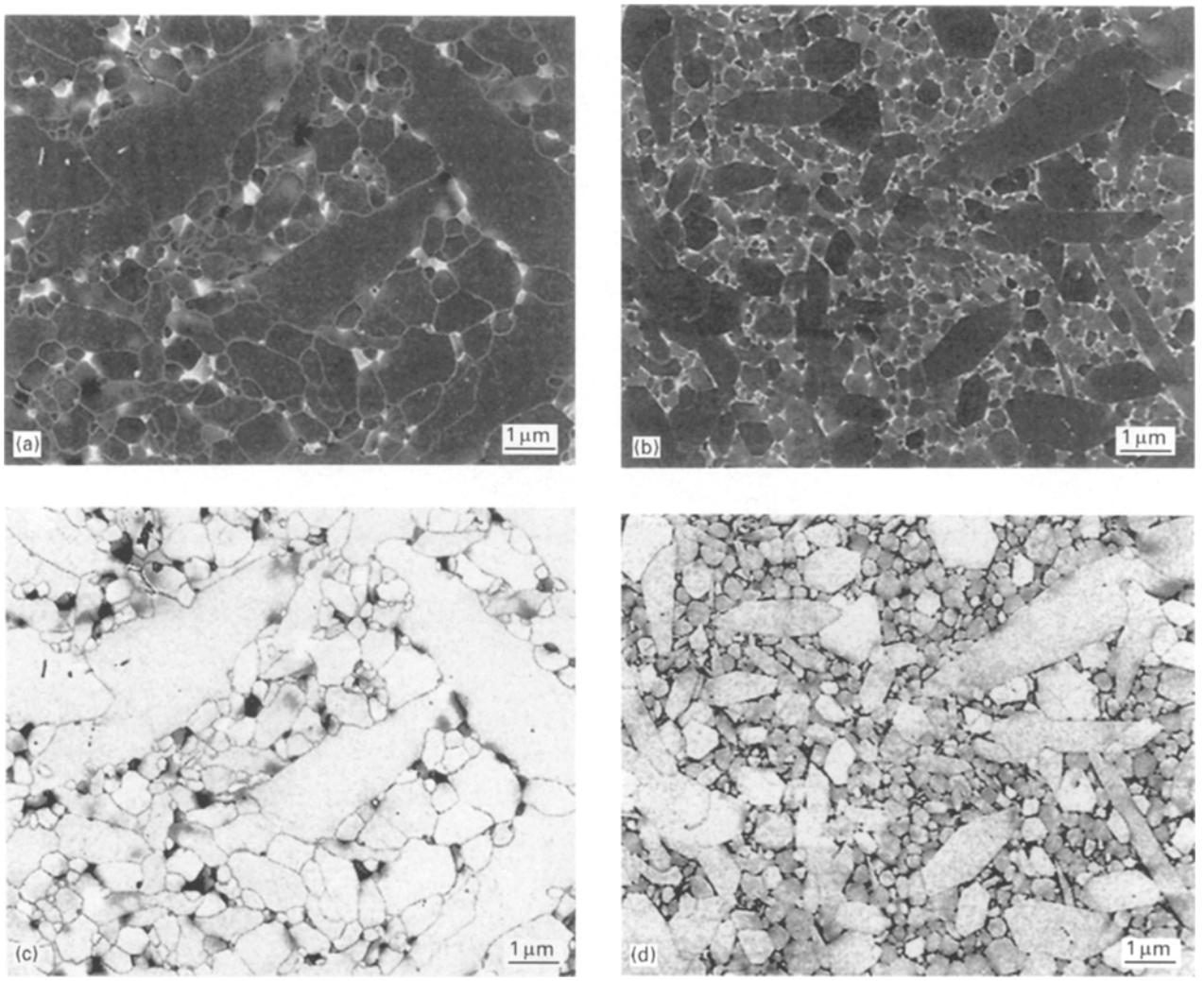

Figure 12 The material that was subjected to a history of reverse cyclic loading exhibited (a) grain growth and more extensive grain-to-grain interlocking of the silicon nitride grains, as seen when compared with (b) the as-received material. Contrast modifications of the micrographs shown in (a) and (b) are shown in (c) and (d), respectively.

associated with the presence of the α silicon nitride will be able to relax the volume of high stress concentration more efficiently than if the material was 100% β silicon nitride. As the high stress concentration is relaxed, the α to β transformation continues which will improve the creep resistance as a consequence. In this example, a high stress concentration (that could conceivably cause slow crack growth and premature on unsuspected fracture) would be relaxed and the creep resistance improved over time, also because of the initial presence of residual α silicon nitride and its associated effects.

A correlation may exist between the value of the time constant for creep relaxation of NCX-5102 silicon nitride at 1370 °C; the frequency of the cyclic waveform; and how the material ultimately undergoes permanent deformation. The authors have suggested in another study (which involved tension–tension cyclic fatigue testing at 1370 °C on a different HIPed silicon nitride) that plastic deformation may only initiate once an anelastic strain threshold is exceeded or saturated [10]. A creep (or strain) relaxation test was conducted at 1370 °C on a NCX-5102 button-head specimen. The creep relaxation behaviour is shown in Fig. 13 corresponding to a stress reduction (that was

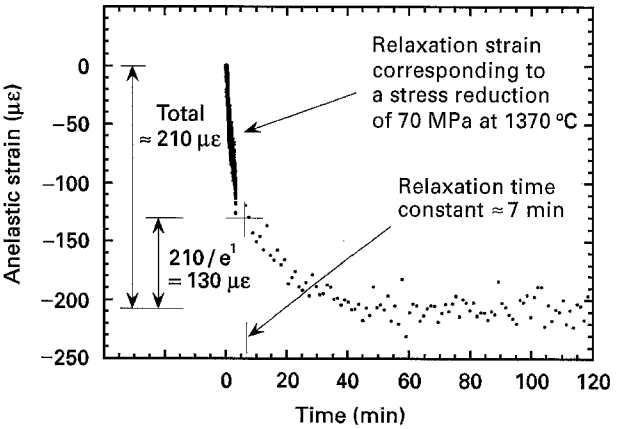

Figure 13 Creep recovery history of NCX-5102 silicon nitride at 1370 °C. Only anelastic, or time-dependent recoverable, strain is shown.

arbitrarily chosen) of 70 MPa (+ 80 − + 10 MPa); elastic strains are not included in the strain values shown. The specimen recovered approximately 210 με (0.021%) anelastic (i.e., time-dependent recoverable) strain. It is assumed that a single time constant (τ) represents the creep relaxation behaviour, then it is

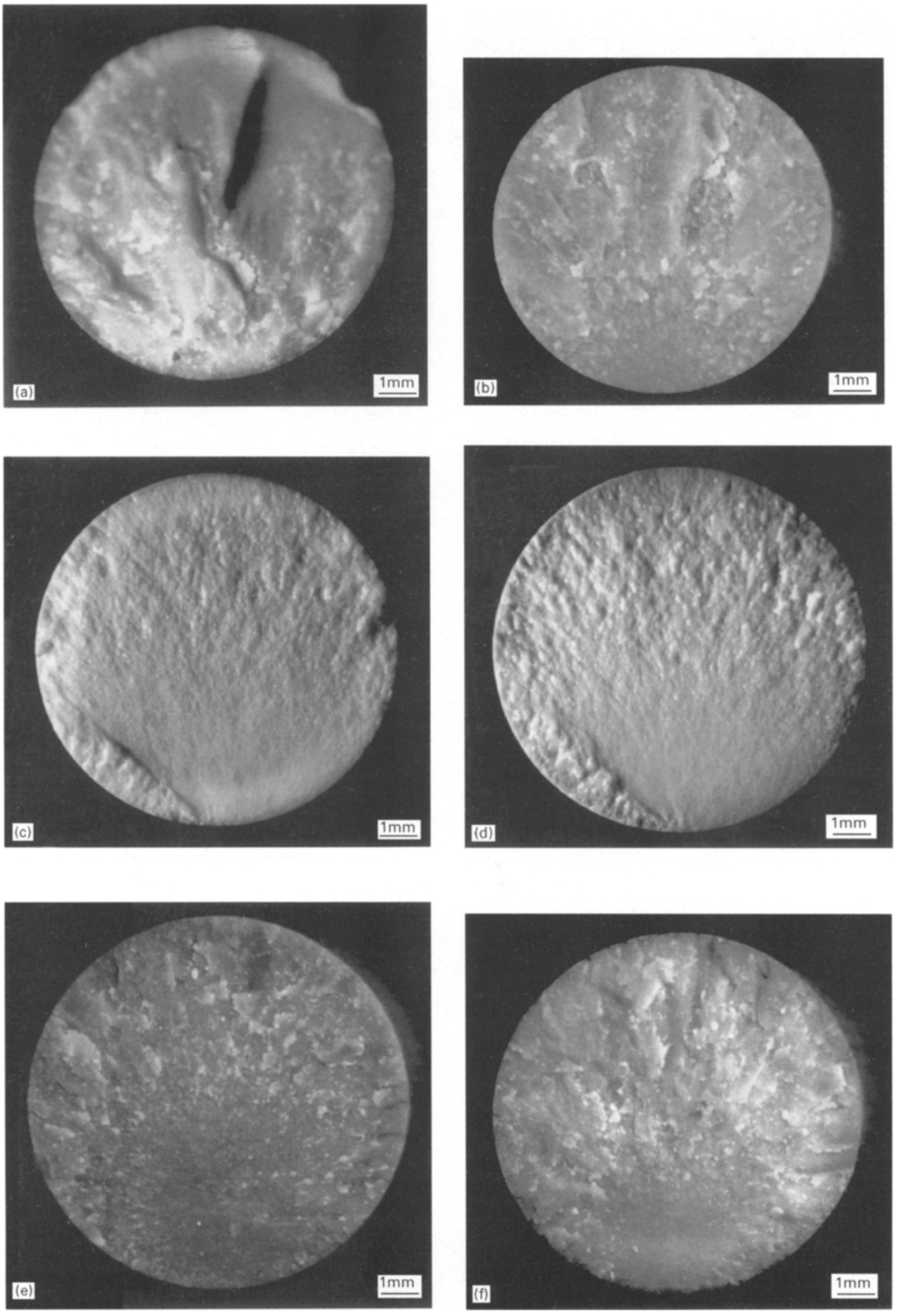

Figure 14 Fracture surfaces of (a) NCX-63, (b) NCX-50, (c) NCX-51, (d) NCX-93, (e) NCX-96, (f) NCX-57, (g) NCX-92, and (h) NCX-111. NCX-63, -50, -96, -57, and -62 failed during cyclic fatigue testing and each fracture surface shows evidence of slow crack growth and mirror, mist, and hackle markings that are indicative of fast fracture. NCX-51, -93, and -111 failed during creep rupture testing after they had been cyclic loaded and each fracture surface shows that fracture occurred as the result of the growth of creep damage zones.

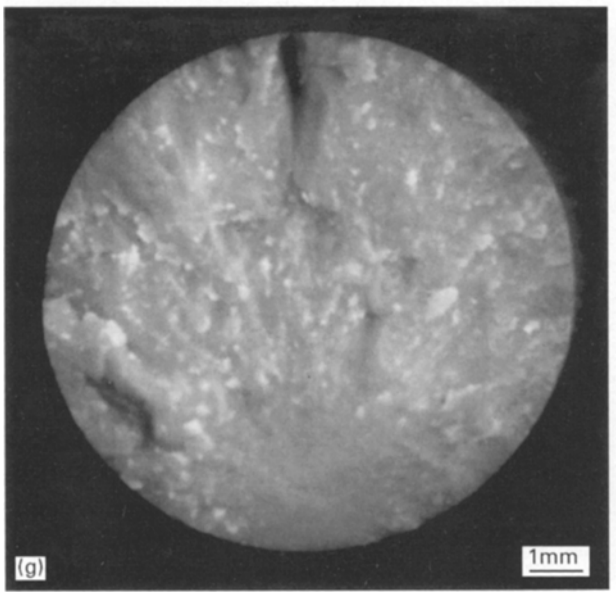

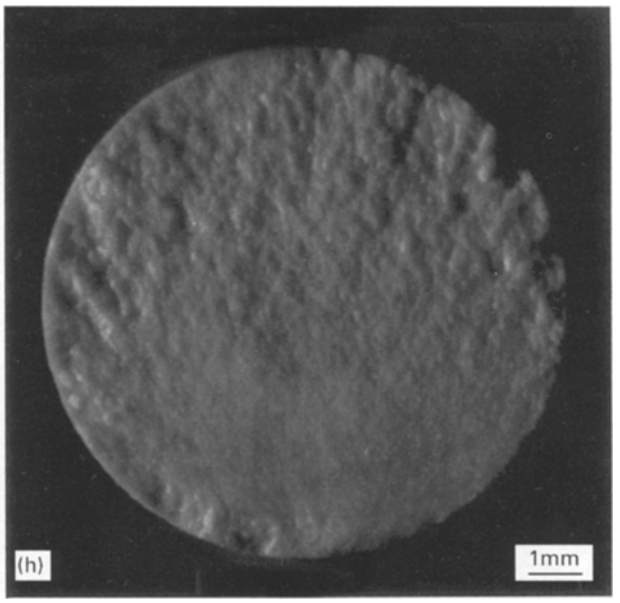

Figure 14 Continued.

estimated from Fig. 13 that τ has a value of approximately 7 min (in tension); where the anelastic strain $\sim K\exp(-t/\tau)$, and where K is a constant and t is time. The amount of relaxed strain will depend on the material's ability to relax strain (represented by τ) and on how much time it has to do so. For the tension–compression cyclic fatigue tests at 1370 °C, the NCX-5102 specimens were loaded and reverse loaded relatively quickly (i.e., 1 Hz) compared to the relaxation time constant and did not have a long period of time to relax anelastic strain. Even the 0.1 Hz tests performed on specimen NCX-111 provided relatively fast loading and unloading compared to this relaxation time constant, although the likelihood was much greater for more creep relaxation in the 0.1 Hz test than the 1 Hz test because its waveform always involved a tensile stress. Under cyclic loading, anelastic strains may not have the opportunity to mature due to lack of time (unlike static creep tests). As a consequence of this, the accumulation of plastic strain is reduced. The insignificant ("insignificant" here referring to the fact that the tensile creep strain that did accumulate during cyclic loading had no apparent bearing on the static creep lifetime of NCX-5102) amount of cavitation that resulted from reverse cyclic loading (see Fig. 9) supports this.

3.4. Fast fracture and creep damage induced fracture

On a macroscopic scale, the original fracture surfaces showed that specimens that failed during reverse cyclic loading failed from slow crack growth (SCG) and subsequent fast fracture, while those specimens that were statically loaded failed from creep-damage. Specimens NCX-63, -50, -96, -57, and -62 failed during reverse cyclic loading and SCG and the resulting mirror, mist, and hackle markings are visible on the original fracture surfaces shown in Fig. 14(a, b, e–g), respectively. Specimen NCX-63 and NCX-50 each failed from SCG at their surface, specimens NCX-57 and NCX-62 failed from near-surface SCG, while specimen NCX-96 failed from SCG in its inner volume.

The SCG regions were macroscopically rough compared with their surrounding mirror regions. An enlarged view of the SCG region that formed within the volume of specimen NCX-96 is shown in Fig. 15. Another example of a SCG region shows a case (specimen NCX-63) in Fig. 16 when it formed at the specimen surface. Unfortunately, oxidation of the original fracture surfaces inhibited microstructural observation of the SCG region (with this problem being especially evident in Fig. 16), so the identification of the flaw, whose presence ultimately led to SCG, was not obtained. Flaws that were associated with the initiation of SCG could have included machining damage and inclusions (extrinsic flaws) or microporosity and amorphous pockets resulting from inhomogeneous crystallization (intrinsic flaws). All four types of flaws have been previously identified in NCX-5102 and have caused failure in room temperature tensile strength tests [14].

Specimens NCX-51 and NCX-93, which were static creep-ruptured after their reverse cyclic loading, failed from creep-damage or stress-corrosion cracking (SCC) that occurred in their near-surface volume. These SCC damage zones are visible (oriented at 6 to 9 o'clock) on the original fracture surfaces of specimens NCX-51 and NCX-93 in Fig. 14(c and d), respectively. The fracture surface of specimen NCX-111, which was cyclic fatigued under tension–tension loading and then creep-ruptured also showed the presence of SCC damage (Fig. 14(h)).

The SCC damage that resulted from creep-rupture testing is categorically different than the SCG that caused failure during reverse cyclic fatigue. Stress-corrosion cracking damage is associated with the silicon nitride's reaction with the ambient environment at elevated temperatures and the accumulation of creep damage (e.g., cavity formation). The evolution of SCG

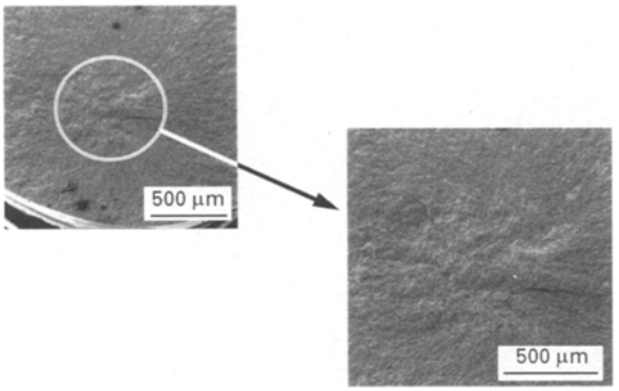

Figure 15 Slow crack growth region on the original fracture surface of specimen NCX-96. NCX-96 failed after 81 cycles at ± 280 MPa at 1370 °C.

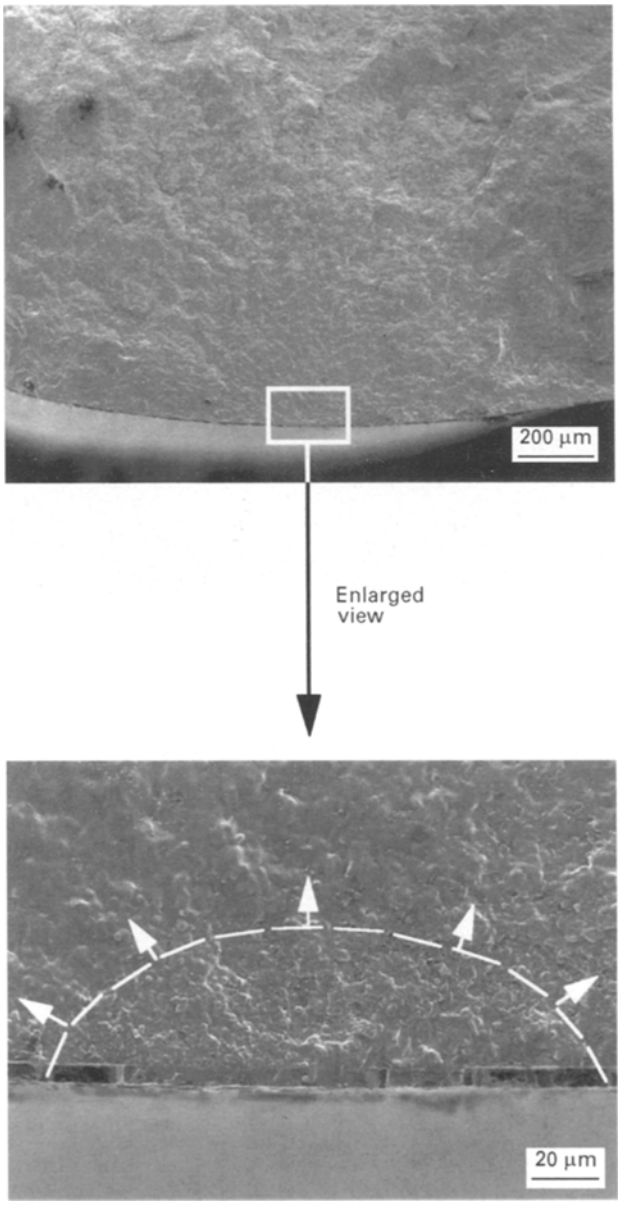

Figure 16 Slow crack growth region on the original fracture surface of specimen NCX-63. NCX-63 failed after a long duration of step-stressing (see Table I), whereupon it failed at ± 290 MPa after 39054 cycles at 1370 °C.

is associated with the presence of the extrinsic and intrinsic flaws described in the preceding paragraph. Although SCC damage and SCG are indeed different, they are somewhat similar in that they both ultimately result in stress-fracture.

Stress-corrosion cracking damage has been examined [18, 22] and its evolution is attributed to many factors, including the applied stress, grain boundary crystallinity, and the amount of impurities present in the grain boundaries of these materials. The size of these macroscopic zones is a function of applied tensile stress [8, 22]. We note that the damage zones on the fracture surfaces of specimens NCX-51 and NCX-93 shown in Fig. 14(c and d) are approximately the same size and that they were creep ruptured at the same static tensile stress of 125 MPa. Perhaps the most intriguing aspect of SCC damage zones is that they are likely to be comprised of highly concentrated pores and cavities present at two-grain and multi-grain junction boundaries; an observation that was arrived at from creep-rupture testing in a non-oxidizing environment [18]. The total accumulation of microcrack coalescence of these local, highly concentrated voids is believed to form the macroscopically large SCC regions.

Similar to the plastic strain argument that was posed in Section 3.3, it is also argued that the activity of SCG in the cyclic fatigue failures and SCC in the creep-rupture failures may be related to the value of the creep recovery time constant and the test-loading frequency. The 1 Hz frequency of the reverse cyclic fatigue tests, coupled with the relaxation time constant of ~ 7 min, shows that the creep recovery process never matures. As a consequence, high stress intensities in the vicinity of extrinsic or intrinsic flaws are not relaxed, and slow crack growth is initiated when the applied stress-intensity is greater than the material's stress intensity threshold. For creep-rupture tests, stress-intensities can be relaxed because the stress is static and ample time is available for the relaxation time to be exceeded. As a consequence of the relaxation time being exceeded: (1) time dependent processes such as cavity nucleation and growth can occur and significant amounts of creep strain can accumulate, (2) microcrack coalescence of the cavities and pores becomes possible, and (3) SCC cracking can evolve and ultimately lead to fracture.

4. Conclusions

Three primary conclusions can be drawn from this study.

NCX-5102 silicon nitride will not fail under reverse cycle fatigue at 1370 °C if the stress amplitude is < 280 MPa and if a sinusoidal waveform is applied at 1 Hz. This threshold stress amplitude is $\sim 60\%$ of the manufacturer's reported average tensile strength for this material at 1370 °C. Slow crack growth will eventually occur at stress amplitudes $\geqslant 280$ MPa and the event of fracture will occur during the tensile stroke of the waveform.

Multi-grain junction cavities resulted as a consequence of the reverse cyclic loading at 1370 °C. Even though the failed, cyclic fatigued specimens endured

half their life under tensile stress and the other half of their life under compressive stress, there was a net gain of cavitation due to tensile creep strain. The presence of cavitation due to tensile creep strain supports the fact that the stress exponent of tensile creep strain is greater than the stress exponent of compressive creep strain in HIPed silicon nitrides.

The static creep resistance of NCX-5102 at 1370 °C will improve if it is first subjected to reverse cyclic loading at 1370 °C for at least 10^6 cycles at 1 Hz (even though some cavitation was present prior to static creep testing). This improvement in creep resistance was likely due to grain coarsening and the activity of extensive grain–grain interlocking; which was ultimately due to the completion of the α to β silicon nitride solution/reprecipitation process that occurred during the history of reverse cyclic loading. It is not discernible from this study whether the reverse cyclic loading history, or the time at temperature, or a combination of both were responsible for the completion of the α to β phase transformation. Even though the NCX-5102 specimens had been subjected to reverse cyclic loading at 1370 °C for $\sim 10^6$ cycles, creep damage was still the dominant failure mechanism (and not slow crack growth) during static creep rupture tests.

Acknowledgements

This research was sponsored by the US Department of Energy, Assistant Secretary for Energy Efficiency and Renewable Energy, Office of Transportation Technologies, as part of the Ceramic Technology Project of the Propulsion System Materials Program, under contract DE-AC05-84OR21400 with Martin Marietta Energy Systems, Inc. The authors thank Dr.'s H.-T. Lin. A.E. Pasto, and J. H. Schneibel for reviewing the manuscript and for their helpful comments and suggestions. The authors thank Dr. H.-T. Lin for performing the plasma etching and Dr. T. R. Watkins for the X-ray diffraction measurements.

References

1. M. VAN ROODE, W. D. BRENTNALL, P. F. NORTEN and G. P. PYTANOWSKI, Paper 93-GT-309, presented at the ASME's International Gas Turbine and Aeroengine Congress Exposition, Cincinnati, OH, May 24–27, 1993.
2. V. M. PARTHASARATHY, J. R. PRICE, W. D. BRENTNALL, G. GRAVES and S. GOODRICH, in the Proceedings of the ASME Turbo Expo '95 Conference, Houston, TX, June 5–8, 1995.
3. J. R. SMYTH, in "*Ceramics and Glasses*, ASM Handbook", Vol. 4, (American Society for Metals International 1991) pp. 995–1002.
4. "*Automative Handbook*" 2nd Edn (Edited by U. Adler, (Robert Bosch GmbH, Stuttgart, 1986) pp. 324–25.
5. M. K. FERBER and M. G. JENKINS, *J. Amer. Cer. Soc.* **75** (1992) 2453.
6. M. K. FERBER, M. G. JENKINS, T. A. NOLAN and R. L. YECKLY, *ibid.* **77** (1994) 657.
7. J.-L. DING, K. C. LIU, K. L. MORE and C. R. BRINKMAN, *ibid.* **77** (1994) 867.
8. M. N. MENON, H. T. FANG, D. C. WU, M. G. JENKINS, M. K. FERBER, K. L. MORE, C. R. HUBBARD and T. A. NOLAN, *ibid.* **77** (1994) 1217.
9. C.-K. J. LIN, M. G. JENKINS and M. K. FERBER, *J. Mater. Sci.* **29** (1994) 3517.
10. A. A. WERESZCZAK, M. K. FERBER, T. P. KIRKLAND and C.-K. J. LIN, in Proceedings of the ASME Turbo Expo '95 Conference, Houston, TX, June 5–8, 1995.
11. M. MASUDA, T. SOMA, M. MATSUI and I. ODA, *J. Ceram. Soc. Jpn Int. Edn.* **97** (1989) 601.
12. A. BUSHBY, F. GUIU, J. KNOWLES and M. J. REECE, *Key Engng Mat.* **89–91** (1994) 673.
13. A. A. WERESZCZAK, M. K. FERBER, T. P. KIRKLAND, E. LARA-CURZIO, V. PARTHASARATHY, and T. T. GRIBB, *Ceram. Engng Sci. Proc.* **16** (1995) 519.
14. V. K. PUJARI, D. M. TRACEY, M. R. FOLEY, N. I. PAILLE, P. J. PELLETIER, L. C. SALES, C. A. WILKENS and R. L. YECKLEY, Development of Improved Processing and Evaluation Methods for High Reliability Structural Ceramics for Advanced Heat Engine Applications, Phase I, ORNL/Sub/89-SB182/1, Martin Marietta Energy Systems, Inc., Oak Ridge Natl. Lab., Oak Ridgae, TN, August 1993.
15. D. J. DEVLIN and K. E. AMIN, *Powd. Diff.* **5** (1990) 121.
16. M. G. JENKINS, M. K. FERBER, R. L. MARTIN, V. T. JENKINS and V. J. TENNERY, Study and Analysis of the Stress State in a Ceramic Button-Head, Tensile Specimen, ORNL/TM-11767, Martin Marietta Energy Systems, Inc., Oak Ridge, Natl. Lab., Oak Ridge, TN, September 1991.
17. W. E. LUECKE, S. M. WEIDERHORN, B. J. HOCKEY, R. KRAUSE, Jr. and G. G. LONG, *J. Amer. Ceram. Soc.* **78** (1995) 2085.
18. A. A. WERESZCZAK, T. P. KIRKLAND and M. K. FERBER, *Ceram. Engng Sci. Proc.* **16** (1995) 901.
19. W. LUECKE, S. M. WIEDERHORN, B. J. HOCKEY and G. G. LONG, in "Silicon Nitride Ceramics: Scientific and Technological Advance, Materials Research Society Symposium Proceedings, Vol. 287, edited by I.-W. Chen, P. F. Becher, M. Mitomo, G. Petzow, and T.-S. Yen (Materials Research Society, Pittsburgh, PA, 1993.) pp. 467–72.
20. H.-T., LIN, P. F. BECHER, *J. Amer. Ceram. Soc.* **74** (1991) 1886.
21. H.-T. LIN, K. B. ALEXANDER and P. F. BECHER, *ibid.* **79** (1996) 1530.
22. A. A. WERESZCZAK, M. K. FERBER, T. P. KIRKLAND, K. L. MORE, M. R. FOLEY and R. L. YECKLEY, *ibid.* **78** (1995) 2129.

Received 7 June 1995
and accepted 13 June 1996